ELSEVIER

Contents lists available at ScienceDirect

International Journal of Heat and Mass Transfer

journal homepage: www.elsevier.com/locate/hmt



Transient heat transfer of impinging jets on superheated wetting and non-wetting surfaces



D. Jacob Butterfield, Brian D. Iverson, Daniel Maynes, Julie Crockett*

Department of Mechanical Engineering, Brigham Young University, 350 Engineering Building, Provo, UT 84602, USA

ARTICLE INFO

Article history: Received 6 October 2020 Revised 23 January 2021 Accepted 2 February 2021

Keywords: Superhydrophobic Jet impingement Boiling heat transfer

ABSTRACT

Superhydrophobic (SH) surfaces possess desirable anti-fouling properties due to low wettability, but have also been shown to reduce heat transfer to subcooled water in impinging jet scenarios. In this work, superheated silicon substrates with varying wettability (hydrophilic or HPi, hydrophobic or HPo, SH) are quenched by an impinging water jet, where the substrate temperature is above the saturation temperature. Silicon wafers are either oxidized to create HPi surfaces, coated with Teflon to make the surface HPo, or plasma-etched and coated to create the necessary micro-texture for SH conditions. All wafers are integrated with an electric resistance heater and then heated to temperatures of 200-320 °C before impingement with an axisymmetric room temperature water jet of varying specified flow rates yielding jet Reynolds numbers between 6000 and 18,000. High-speed visual data is collected, showing how the lamellar liquid contact region, limited by thermal breakup due to boiling, grows radially as the surface cools to temperatures below saturation. This data is correlated to temperature data recorded on the back side of the wafer using a thermal camera. Results of this study confirm previous conjecture that surface wettability can alter maximum heat flux, which is quantified here for the described scenario by up to 40%, and can also affect jet thin film spreading by up to 50%. Increasing initial surface temperature decreases thin film spreading rate on all surfaces, and increases heat transfer on all but the SH surfaces. Increasing Reynolds number yields an increase in heat flux, and affects both the thin film spreading rate as well as the maximum radius of the thin film region.

© 2021 Elsevier Ltd. All rights reserved.

1. Introduction

Liquid jet impingement is utilized in many cooling applications due to the highly convective thin film which occurs as the jet spreads on the surface, providing significant heat transfer from a surface [1]. This method of heat transfer finds application in metal processing [2], piston cooling (with oil as the working fluid) [3], gas turbine cooling [4], and emergency nuclear reactor cooling [5]. Other important applications for jet impingement include electronics cooling, rocket launchpad cooling, and rocket nozzle or jet turbine cooling. One common issue in many of these industrial applications is that the ability to transfer heat is reduced when fouling occurs due to water evaporation on the heated surface which can lead to an accumulation of trace chemical residuals [6]. Operations are interrupted in order to clean these surfaces, which further inhibits production or performance.

Superhydrophobic (SH) surfaces are a potential solution for the issue of fouling [7]. Water-repelling SH surfaces are manu-

* Corresponding author.

E-mail address: juliecrockett@byu.edu (J. Crockett).

factured by altering surface geometry to provide micro- or nanoscale roughness (as shown in Fig. 1a), and by changing the surface chemistry to reduce surface energy, making it inherently hydrophobic. With this combination of surface modification, water only contacts the highest points of the rough surface, and air gaps are left beneath the liquid, reducing the aggregate adhesive force and causing the water to bead up (interior static contact angle greater than 150°). Such low adhesion between the water and surface enables high droplet mobility. Water droplets will readily roll from surfaces, improving anti-fouling properties as water will not remain to evaporate on the surface after impingement.

Prior works addressing the use of SH surfaces in jet impingement cooling have emphasized steady-state hydrodynamics and low temperature heat transfer, showing that increasing hydrophobicity leads to a smaller hydraulic breakup radius of the thin film region [8] and reduced convective heat transfer [9]. Here, the usefulness of micropost-patterned (see Fig. 1a) SH surface implementation in transient jet impingement heat transfer situations at superheated wall temperatures is explored.

A schematic illustration of the radial cross-section of an impinging jet on a superheated surface is shown in Fig. 1b. After ini-

Nomenclature а iet radius specific heat c_p thermal conductivity k Q volume flow rate q'heat flux radial distance from stagnation point r Reynolds number = Q/(va)ReD temperature Τ time t velocity υ δ wafer thickness emissivity 6 ν kinematic viscosity density ρ Н heater i jet S surface si silicon w water

tial impingement, the following regions exist (shown in Fig. 1b): a center region of high stagnation pressure; a liquid lamellar region or thin film where convective heat transfer is dominant; a boiling front (r_f) where phase-change heat transfer is dominant and thin film spreading is restricted by high temperature differences; and a droplet ejection region where droplets move outward, levitating on a self-generated vapor layer.

Heat transfer behavior of impinging jets in single-phase convection [10-14], nucleate boiling (vapor bubbles generated at the heated surface), and transition and film boiling in steady-state conditions have previously been investigated. Robidou et al. showed experimentally that heat transfer improves markedly as the nucleate boiling condition is reached and then diminishes when transition boiling conditions prevail [15]. Previous authors have experimentally explored several parameters with relation to boiling jet impingement heat transfer, such as increased heat transfer with increased jet subcooling [2,16,17]. Increasing jet velocity has also been shown repeatedly to promote higher heat transfer [18,19]. There is a negligible impact of jet length (nozzle-to-surface spacing) for boiling scenarios [15], and spatial variation in the radial direction shows decreasing heat flux further from the stagnation point [20]. Others have explored theoretical models based on these parameters, with similar general results [21-23]. A review of the

literature regarding nucleate boiling during jet impingement has been previously conducted [24].

Several studies have also investigated the transient effects of quenching superheated metal surfaces. This has shown a dependence on surface material properties [25], and introduces a scenario where convective, nucleate, transient, and film boiling heat transfer can all occur at various points and times across a surface. Similar results to steady-state cases, in regards to increased subcooling and higher flow rates leading to higher heat transfer, were also observed for transient cases [26–28]. In these transient studies, several experimental techniques have been utilized in order to acquire the time-dependent data necessary for heat transfer calculations, including the use of thermocouples [29–31] or by balancing the average heat removed with the supplied heat [32]. Both of these techniques have limited spatial resolution of data acquisition, and newer methods such as using high-speed thermal cameras have been shown to improve accuracy [33].

A single paper has been published regarding the impact SH properties exert on the effectiveness of jet impingement heat transfer [9]. In this work, Searle et al. created a model to predict the local Nusselt number for various spatial regions along the surface for sub-critically heated surfaces and found that with increasing surface cavity fraction (ratio of etched microfeature surface area to total surface area), a lower heat transfer rate was observed. Reduced heat transfer occurs because the air gaps formed beneath the impinging liquid and between microstructures act as an insulating layer to heat transfer. However, the work by Searle et al. only dealt with single-phase forced convection, which is not the primary mode of heat transfer at temperatures above saturation.

Research focused on SH surfaces at temperatures above saturation has been explored for droplet impingement scenarios. Clavijo et al. found that the water vapor generated beneath the droplet during impact could escape through the SH microstructures such that there was little to no nucleate boiling on the SH surfaces [34]. Instead, film boiling and Leidenfrost behavior was observed over a broad range of impact conditions [35]. Similar effects were also observed in pool boiling experiments [36]. As surface temperature increases above the fluid saturation temperature in jet impingement quenching scenarios, a boiling region occurs that restricts spreading of the liquid thin film. Due to local rapid phase change, water droplets in this region begin to elevate above the surface due to the local generation of vapor. Since there is very little attraction between water and SH surfaces initially, the Leidenfrost effect occurs more readily [37]. However, for microstructured surfaces that are natively hydrophilic, or superhydrophilic, Qiu and

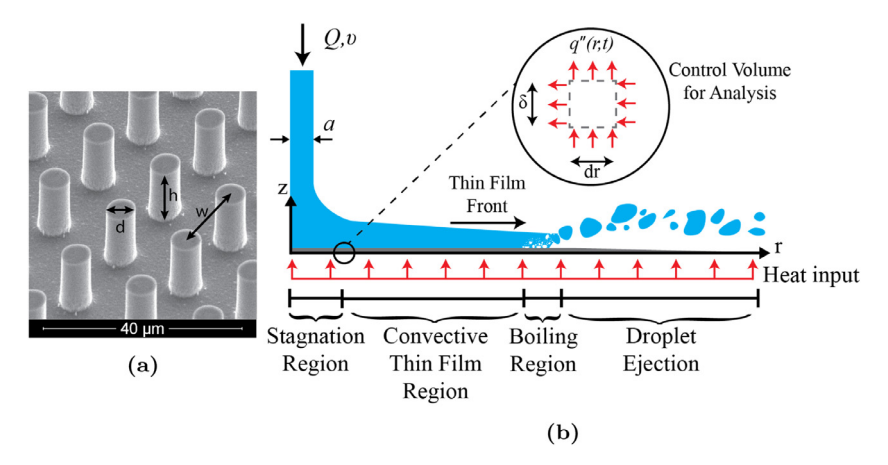


Fig. 1. (a) SEM image of post microstructures on a SH surface. (b) Radial cross-section view of a perpendicular impinging jet on a heated surface. An insert shows the differential control volume used to calculate heat flux from the surface to the water up to the thin film front, r_f .

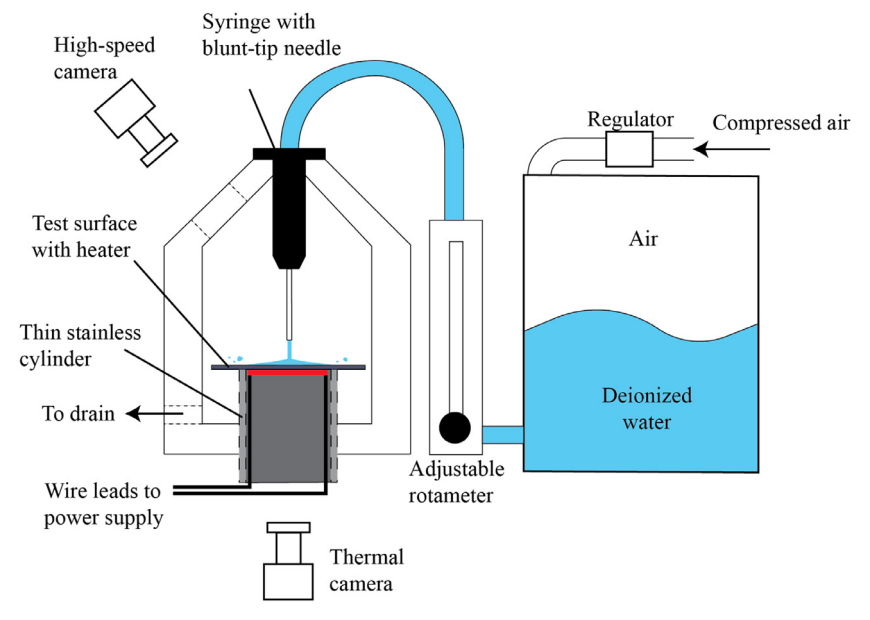


Fig. 2. Schematic of experimental apparatus.

Liu reported heat fluxes 30% higher due to the lower contact angle and increased contact area [38]. These data confirm wettability and microstructure have a significant effect on jet impingement heat transfer in the superheated regime.

Potential trade-offs remain to be clarified between the desirable anti-fouling properties of SH surfaces and reduced heat transfer effectiveness of film boiling. Here, jet impingement experiments are performed to compare boiling heat transfer during quenching on superheated SH surfaces to that for hydrophilic (HPi) and smooth hydrophobic (HPo) surfaces (no surface structuring). The jet Reynolds number is defined as $Re_D = Q/(\nu a)$ where Q is the jet volumetric flow rate, ν is the kinematic viscosity of water and a is the jet radius. Influence of Re (6000 < Re < 18,000) and initial surface temperature (200 $^{\circ}$ C $< T_0 < 320 ^{\circ}$ C) on the thermal transport physics are explored. Results are presented showing that SH conditions have a significant impact on cooling dynamics during jet impingement if the surface is superheated, which was previously undiscovered. Further, SH surfaces can yield increases in thin film spreading time by up to 170% and decreases in the maximum heat flux by up to 70%, compared to behavior for a HPi surface.

2. Methodology

This section describes the experimental apparatus, data acquisition, and data analysis techniques used in this study. The experimental apparatus and methodology used to collect data was similar to that of Searle et al. [39] and are briefly summarized. Important differences of operation due to transient behavior and much higher surface temperatures are noted.

2.1. Experimental apparatus

There are three main components that comprise the experimental apparatus: the surfaces and heating elements, the jet and associated hardware, and the cameras. A schematic of the apparatus is shown in Fig. 2.

An oxidized silicon wafer with diameter of 100 mm and thickness $525 \pm 5 \,\mu m$ was used for the standard (HPi) case. Using a digital goniometer, the static contact angle with water was measured at nominally 55° . The back side of each surface was screen-printed with a silver paste (ESL 599-E) to create an integrated electrical

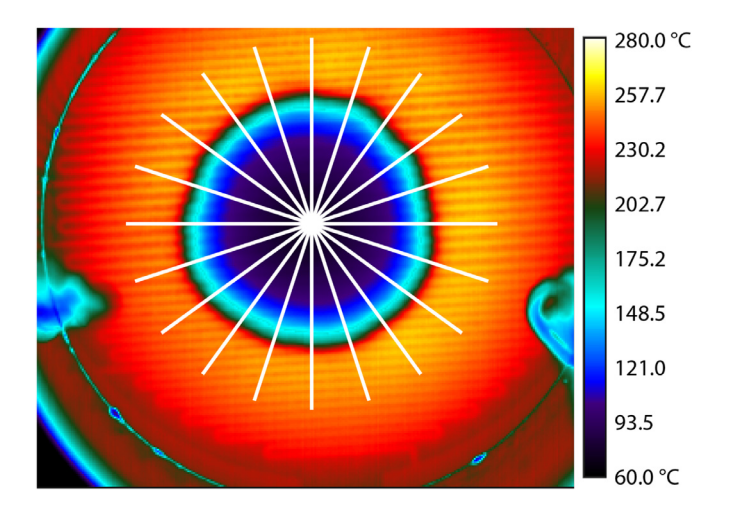


Fig. 3. Thermal camera image of temperature across the back side of a wafer. The alternating red and yellow lines are caused by the resistance heater, and the darker area shows the progression of the jet across the surface. White data-averaging radial lines are also shown. (For interpretation of the references to color in this figure legend, the reader is referred to the web version of this article.)

resistance heater. The heater was designed to have a coverage area with nominal diameter of 50 mm, providing 0.25 Ω of resistance through a series of thin traces nominally 0.5 mm thick (see horizontal heated lines in Fig. 3). Leads were attached to the heater using a conductive epoxy (Atom Adhesives AA-DUCT 2979) connecting it to a 20 V, 120 A maximum DC power supply (HP 6011A). A thin layer of flat black coating (Rustoleum® 248,903) of known emissivity ($\epsilon = 0.97$) was spray painted on the entire back of the wafer, covering the heater and allowing for thermal imaging to determine the temperature across the back side of the wafer over time. This paint layer negligibly affected the temperature measurement, which was confirmed by comparing the temperature reading from the IR camera of the bottom of the surface with the temperature reading from a thermocouple placed on the top surface. The difference in the readings was nominally 1% of the IR camera measured temperature.

HPo surfaces were created by coating the top surface of an oxidized silicon wafer with a thin layer (100 nm) of chromium

via electron-beam evaporation followed by a thin layer (200 nm) of natively hydrophobic DuPontTM Teflon® (commercial brand of polytetrafluoroethylene, PTFE). Teflon was spin-coated onto the surface at 1000 rpm for 20 s, resulting in static water contact angles of 120°, as measured by a goniometer.

The SH surfaces were fabricated by first patterning surface features onto the same type of silicon wafer used for HPi and HPo surfaces using standard photolithography methods. A small, 6 mm diameter circular "target" was left unpatterned at the center of the wafer to prevent wetting in the jet stagnation region. After patterning, wafers were etched using reactive ion etching (RIE) to create microscale posts with a pitch of 16 μm , diameter of 7 μm , and depth of 25 μm (see Fig. 1a). This resulted in a cavity fraction of nominally 85%. Etched silicon wafers were then rendered SH with a Teflon coating and screen-printed with the integrated heater described previously. SH surfaces that were fabricated for this study exhibited a static contact angle of 155 $\pm\,4^\circ$.

To provide a fully developed impinging jet, a long (15 cm) stainless steel blunt-tip needle with inner radius $r_j = 1.275\,$ mm was placed nominally 5 cm above the wafer. Upstream the nozzle was connected to a rotameter which was attached to a pressure tank containing deionized water. This allowed for an adjustable jet flow rate and controlled the jet Re_D. The wafer was placed on a hollow, thin-walled stainless steel cylinder which inhibited conduction from the wafer due to its relatively low thermal conductivity and thin supporting upper rim. The water emptied from the edges of the wafer into a 3D-printed plastic collection container that also supported the entire subsystem.

A thermal camera (FLIR® SC6100) recorded temporally varying temperature data at a frame rate of nominally 200 Hz. The camera resolution was 320×256 pixels over a viewing window of approximately 55×45 mm. Data was analyzed only over this viewing window as it was sufficient to examine the wafer area covered by the heater. High-speed images were also taken with a Photron Fastcam APX RS located above the wafer at an angle of about 40° normal to the surface. The high-speed images were acquired at a frame rate of 500 Hz with a spatial resolution of 1024×1024 pixels over a viewing window of nominally 70×70 mm. High speedimages were primarily used to estimate the development of the thin film front, $r_f(t)$, which is defined as the location of thin film breakup. This is estimated visually along the centerline of the image and the two radial values are averaged resulting in an accuracy of ±0.3 mm for r_f .

2.2. Data acquisition

Test surfaces were electrically heated until the maximum surface temperature reached the prescribed value, after which jet flow was initiated and an electronic trigger to both cameras was enabled. Values for initial surface temperature and jet Re_D are given in Table 1. Synchronized visual and temperature data was then collected. A sample image of thermal data collected beneath a wafer is shown in Fig. 3. The temperature signature of the thin film heater is visible in the hottest regions as thin horizontal lines, but its effect was accounted for as explained later. The region where liquid is in contact with the surface is apparent by the significantly lower temperature at the center. The edge of this region is nomi-

Table 1 Experimental parameters.

Parameter	Units	Values	Uncertainty
Surface Type	–	HPi, HPo, SH	$ \pm 4^{\circ}$ $\pm 3^{\circ}$ C $\pm 0.5 \times 10^{3}$
Static Contact Angle	deg,	55, 123, 155	
Initial Temperature	∘C	200, 280, 320	
Jet Re _D	–	6, 12, 18 (×10 ³)	

nally where the temperature gradient is highest, both spatially (the highest transition in temperature in Fig. 3) as well as temporally, and has been shown to be a good approximation for the thin film spreading front [40]. Since the heater does not cover the entirety of the wafer, there is an initial small variation of temperature across the surface, with the highest values near the center, and lower temperatures outside the heater radius.

2.3. Data analysis

Local heat flux from the wafer to the jet, q'', was also calculated as a function of radius, r, and time, t, by first averaging the radial temperature data over 20 equally-spaced radial lines (shown in Fig. 3), which helped reduce error (beyond 20 radial lines the mean change in temperature is less than 1%). Then, q''(r,t) was found by numerically solving the energy balance of Eq. (2) for a local control volume as illustrated in Fig. 1b:

$$q''(r,t) = \frac{\delta}{r} \frac{\partial}{\partial r} \left(k_{\rm si} r \frac{\partial T}{\partial r} \right) + \frac{q_{\rm H}}{\pi r_{\rm H}^2} - \delta \rho c_p \frac{\partial T}{\partial t}$$
 (1)

where q'' is the instantaneous local heat flux from the surface to the fluid as a function of *r* and *t*. The first term on the right hand side represents conjugate heat transfer through the wafer in the radial direction, where δ is the wafer thickness and k_{si} is the thermal conductivity of silicon as a function of the measured local surface temperature, T. The next term consists of the heater input, q_H divided by the heater coverage area, where r_H is the radius of the heater regions. The last term represents transient storage of energy in the wafer and is a function of the silicon properties of density, ρ , and specific heat, c_p , as well as T and t. After experimentation, it was determined that the heater input was at least two orders of magnitude lower than the other terms and was therefore deemed negligible during the initial quenching process (for times less than 1 s). Heat loss during impingement due to natural convection and radiation on the back side of the wafer was also neglected as it was orders of magnitude smaller than the other terms.

The measured T(r,t) was used to calculate q''(r,t) by numerically solving Eq. (1). Attempting to evaluate the temporal and spatial derivatives of T(r,t) necessary for Eq. (1) amplifies the measurement error due to the spatial and temporal resolution. This was mitigated by fitting lines to the data and estimating derivatives from this line. Specifically, a quadratic fit to the temperature data locally was generated using a sliding, seven-point range of data through time. The derivative in time was then calculated from this fit line and averaged with the corresponding calculations on each of the 20 radial lines to mitigate effects of localized heating due to the presence of heater lines. This value was then used as $\partial T/\partial t$ in Eq. (1). For the spatial derivative, groups of 31 sequential temperature readings along each radial line were fit to secondorder curves. Again, the local derivative from these curve fit was averaged with the corresponding radial location from each of the other 20 radial lines and the resulting value was used as $\partial T/\partial r$ in Eq. (1). After q''(r,t) was calculated, Fourier's 1D conduction law $(q'' \approx -k_{si}(T_s - T_b)/\delta)$ was used to correct the top surface (T_s) temperature using the silicon thermal conductivity (k_{si}) , local heat flux (q''), and wafer thickness (δ) . An average of the top and bottom temperatures was then used to recompute the local heat flux from the heated wafer to the water.

The measured temperature data was also examined by computing the total energy transfer rate from the surface, E(t), as the thin film spreads over time:

$$E(t) = \int_0^t \int_0^{r_{lim}} 2\pi r \delta \rho c_p(T(r,t) - T_j) dr dt$$
 (2)

where r_{lim} is a standard radius over which integration is performed for each case (set to be 20 mm as uncertainty increased beyond

this point, and the full heater radius was not encompassed in the viewing window) and T_j represents the initial temperature of the jet. The derivative of E(t) throughout time also provided an average heat transfer rate from the surface to the water across the viewable area of the wafer (nominally $0 \le r \le 20$ mm). The value of E(t) computed from Eq. (2) was normalized, $\hat{E}(t)$ by the total initial thermal energy stored in the wafer over the same radial extent (Eq. (2) with $T(r,t) = T_0(r)$) in order to compare surfaces with varying initial temperature.

Potential sources of uncertainty impacting calculations include temperature measurements, which have $\pm 1.2\%$ uncertainty based on a 95% confidence interval in averaging as explained above and $\pm 1\%$ manufacturer-reported instrumentation error. There is also some uncertainty in the wafer specific heat and thermal conductivity as functions of temperature, based off curve fits to measurements of these properties. Error in spatial calibration and correlation was between ± 0.6 and 1.1%. Performing a standard root-mean-square propagation of error analysis of the contributing components in Eq. (1) resulted in an uncertainty on the output heat flux of $<\pm 5\%$. Table 1 presents experimental conditions that were varied in this study and the typical uncertainties in the measured values.

3. Results and discussion

Fig. 1 b illustrates jet impingement quenching of a surface, where the jet rapidly transitions into a radially expanding liquid thin film and concomitantly the surface cools rapidly. This behavior was captured in the high-speed images shown in Fig. 4, which will be discussed in detail below. Localized boiling occurs in the vicinity of the thin film edge, and correspondingly the heat flux attains a local maximum at this position (see corresponding data at the bottom of Fig. 4). This section of the paper presents qualitative and quantitative results that demonstrate the quenching behavior is altered dramatically when the target surface is SH. Specifically, the results show that the spreading speed of the expanding thin film is notably slower on the SH surface. Further, the maximum instantaneous thermal transport is smaller on the SH surface. As a consequence of these two dynamics, the quenching time for the SH surface is appreciably longer than for the smooth HPi or HPo surfaces.

Initial surface temperature and jet Re_D also influence the transient thermal transport between the surface and the water. The effects of these parameters was similar for all surface types, and in general followed trends and orders of magnitude previously examined for HPi surfaces [26–28]. First we consider the hydrodynamics of thin film spreading as a function of initial surface temperature, jet Re_D , and surface type, and quantify spreading times for each scenario. Subsequently, the heat transfer rate is quantified from the measured temperature data, following the approach discussed above, for the same scenarios. Finally, qualitative observations regarding wetting of the surface microstructure during the transient process are provided.

3.1. Hydrodynamics

Images depicting jet impingement at t=0, 0.05, and 0.1 s after the start of impingement are shown in Fig. 4 for the SH, HPo, and HPi surfaces at the same initial temperature ($T_0=T(t=0\,\mathrm{s},\,r=0\,\mathrm{mm})=320\,^\circ\mathrm{C}$) and for the same jet Re_D (12,000). At $t=0\,\mathrm{s}$ the unpatterned center target region of the SH surface is clearly visible. Unlike the SH surface, the HPi and HPo wafers had no microscale roughness added and thus retain their original mirror-finish. The light streaks in the background on these surfaces are reflections of the surroundings. Also shown at the bottom of Fig. 4 are plots

showing the local wafer temperature and heat flux for the SH surface at the same three instants in time.

The thin film region, which forms after water contacts the surface, is clearly seen at t = 0.05 and 0.1 s as the round, glassy region in the center of the image surrounded by a spray of droplets lifting off the surface as the water boils. As mentioned before, a boiling region formed on all superheated wafers that were tested in this study, but the impact on the spreading behavior varied with surface type. Liquid water only contacts the surface in regions where the wafer is cooled below a sustainable film boiling temperature. An enhanced Leidenfrost effect was expected to occur with the SH surfaces due to the non-wetting hydrophobic microstructure, which allows a stable vapor layer to form beneath the liquid between the posts, as has been seen with pool boiling, microchannel flow and droplet impingement research [34,36,37]. The images of Fig. 4 reveal that the thin film region is smallest for the SH surface compared to the other surfaces at the same time due to this enhanced effect. The spreading rate of the thin film region impacts heat transfer because it alters how rapidly water contacts and cools a surface (more rapid spreading facilitates more rapid heat transfer).

As shown in the images and the T(r,t) and q''(r,t) data shown at the bottom of Fig. 4, the thin film front location measured with high-speed imaging is at approximately the same radius as the measured maximum local heat flux. Fig. 5 shows the normalized instantaneous radial position of the thin film front (r_f/a) determined from the high-speed images as well as the normalized location of maximum heat flux (r_q/a) for all three surfaces. The data of Fig. 5 correspond to $T_0 = 320$ °C and $Re_D = 12,000$, but all other cases show similar trends. The instantaneous edge of the thin film, selected from the high-speed images, is shown with hollow blue markers (left axis) and the maximum heat flux location is shown with solid red markers (right axis). Locations of the edge of the jet radius and SH target radius are shown with blue and gray shading for reference. Nucleate boiling, which typically demonstrates the highest heat flux, occurs over a finite region, but the peak in heat flux occurs at the center of this nucleate boiling region. The thin film front forms slightly beyond this point radially as transition boiling and film boiling begin to dominate. The maximum heat flux location is thus always slightly smaller than the measured thin film location, consistent with previous findings [41,42]. However, since the two locations are very close, the location of maximum heat flux is employed in subsequent comparisons presented here.

The thin film spreads most rapidly on the HPi surfaces and thus for the same instant in time the initial interfacial contact between the surface and the thin film is the greatest for this surface. In contrast, the spreading rate is slowest on the SH surface, due to the enhanced Leidenfrost effect. Fig. 6 compares the measured time, t_f , for the thin film to spread 4, 8, and 12 jet radii from the stagnation point for the three different surfaces. The left panel of the figure shows results at $T_0 = 200$, 280, and 320 °C (all at Re_D = 12,000), while the right panel shows results at Re_D = 6000, 12,000, and 18,000 (all at $T_0 = 280$ °C). Shorter data bars indicate a shorter time to reach the corresponding normalized location on the wafer, or faster spreading and greater liquid contact. For all cases, the fastest and slowest spreading occurred on the HPi and SH surfaces, respectively. For example, at $T_0 = 200$ °C, t_f for 12 jet radii was 63% lower for the HPi case compared to the SH surface. Indeed, for all values of n (4, 8, and 12), t_f was always largest on the SH surface and this behavior was enhanced as T_0 increased. This increase in t_f quantitatively supports the idea that SH surfaces generally enhance Leidenfrost conditions, delay thin film spreading and suppress boiling. The net result should be an overall slower rate of surface cooling. Results for the HPo surface show that for n = 4 and 8 the HPo and HPi surfaces yield similar t_f values, although they are always slightly greater for the HPo surface. At n = 12, however,

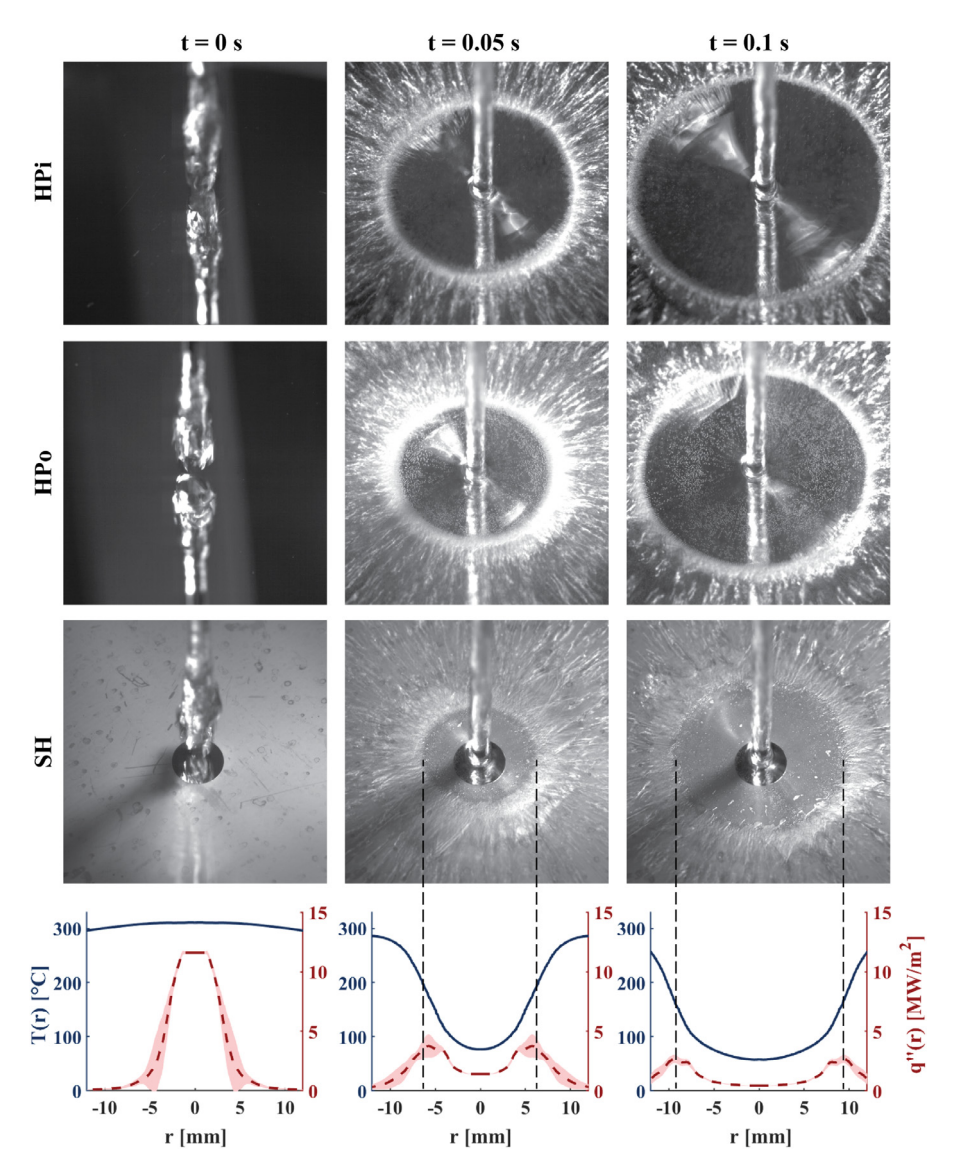


Fig. 4. Images showing impingement at multiple times on the HPi (top), HPo (middle) and SH (bottom) surfaces with $T_0 = 320$ °C and Re_D = 12,000. Temperature and heat flux as functions of time and radial position are also shown for the SH surface, with shaded regions indicating typical uncertainty.

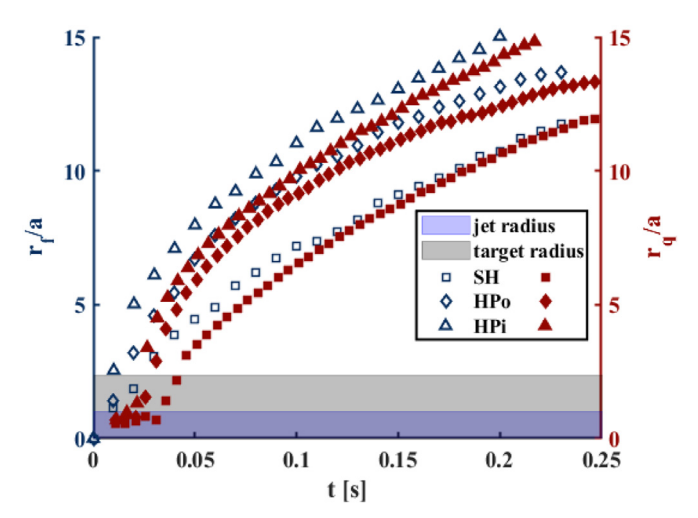


Fig. 5. Non-dimensional thin film radius (r_f/a) and location of maximum local heat flux (r_g/a) as functions of time and surface type for $T_0 = 320$ °C and Re_D = 12,000.

 t_f on the HPo surface showed greater deviation from the HPi data. Comparing HPo surface behavior to that of SH surfaces shows that adding surface roughness results in slower thin film spreading for inherently hydrophobic surfaces.

The influence of jet Re_D on t_f is illustrated in Fig. 6b. In general, increasing the inertia of the subcooled liquid yields faster cooling and spreading, regardless of surface type. As Re_D increases, t_f decreases, although this effect appears to diminish with increasing Re_D . Note that at $Re_D = 6000$, the thin film never spreads to 12 radii for any of the surfaces. Further, for the SH surface, the film never even reaches 8 radii. This occurs because the film breaks up into droplets at a point where the jet momentum is balanced by the inward pull of surface tension on the film, which occurs at smaller radial positions as ReD is decreased. This is visualized in Fig. 7, where instantaneous images at times much greater than 0.1 s are shown with Re_D of 6000 and 12,000. At Re_D = 12,000 the maximum spread radius is 2.6 times greater than for the $Re_D = 6000$ case. In this work the maximum thin film radius was always greatest for the HPi surfaces and smallest for the SH surfaces.

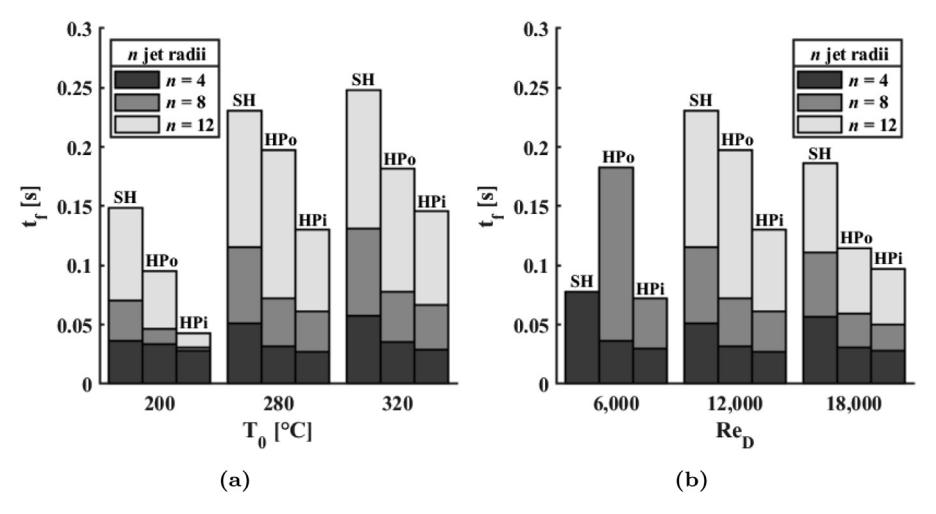


Fig. 6. Time for the jet thin film radius to reach various radii downstream from the stagnation point (t_f) as a function of (a) T_0 (Re_D = 12,000) as well as (b) jet Re_D $(T_0 = 280 \, ^{\circ}\text{C})$.

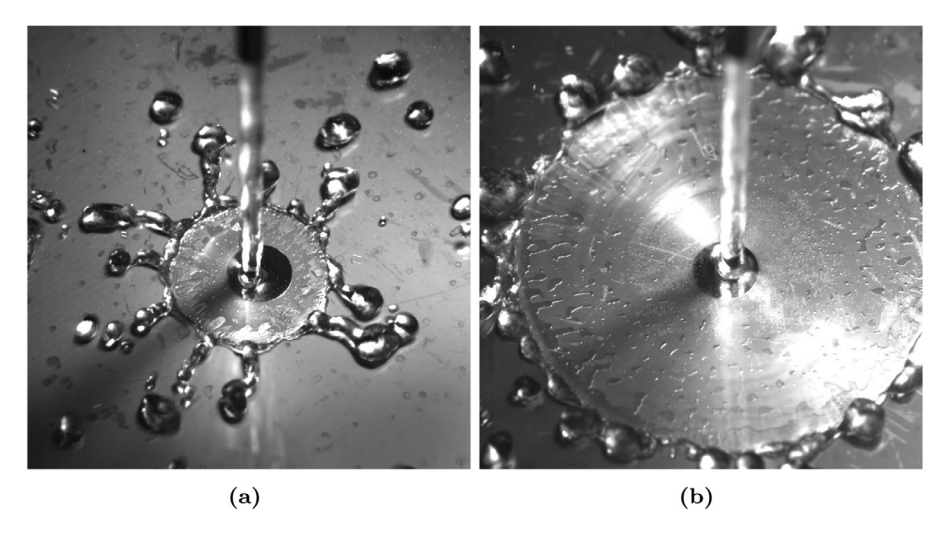


Fig. 7. Maximum thin film spreading for the SH surface at (a) $Re_D = 6000$ and (b) $Re_D = 12,000$, with $T_0 = 280$ °C.

3.2. Heat transfer

The temperature and heat flux data shown at the bottom of Fig. 4 for the SH surface reveals the following important points. First, the surface cools rapidly at the center of the wafer and q'' is a maximum at t=0 s and r=0 mm (stagnation point). Second, with increasing time the surface cools and approaches the temperature of the impinging jet in the thin film region, where q'' also decreases rapidly. The vertical dashed lines shown for t=0.05 and 0.1 s mark the edge of the thin film region, which also corresponds to the boiling front. This is shown in the high-speed images of Fig. 4 as the white or lighter region where droplets are ejected from the surface. The local heat flux is at a maximum value (for t>0 s) just inside the boiling or thin film front.

Surface temperature as a function of time and radial position for the SH surface is shown in a 3-D plot in Fig. 8a for Re_D = 12,000 and T_0 = 320 °C. As expected, the stagnation region (r = 0 mm) cools much more rapidly compared with outer radial positions. Large temporal and spatial temperature gradients are evident as the surface rapidly cools due to the spreading thin film. The higher surface temperature far from the stagnation point suggests that droplet movement past the surface beyond the edge of the thin film (shown in Fig. 4) exerts negligible influence on surface cooling. Fig. 8b shows the instantaneous local heat flux for the

same conditions and parameters as Fig. 8a and shows more clearly how the SH wafer cools. Thermal energy is transferred due to spatial and temporal temperature gradients and the peaks in heat flux correspond to the locations in Fig. 8a where the temperature gradients are a maximum. Starting with the maximum heat flux at r=0 mm and t=0 s, the peak heat flux decreases in magnitude with increasing time due to the decreasing difference in surface and jet temperatures. The peak heat flux also decreases with increasing radial location as the thin film spreads and heats up, again lowering the temperature difference.

Instantaneous heat flux for the HPo and HPi surfaces are shown in Fig. 8c and d, respectively, for the same Re_D and T_0 . Similar overall trends exist for all surfaces. The initial heat flux is highest for the HPi surface (d) and it cools more rapidly than do the SH (b) or HPo (c) surfaces, as evidenced by the strong curvature in the heat flux peak with increasing time. More quantitative heat flux data will be compared for the three surfaces later in this section.

Fig. 9 provides the surface temperature and local heat flux as functions of radial position for all surface types at three different times: t=0, 0.05, and 0.15 s. The curves shown represent temporal slices of the 3-D plots shown in Fig. 8 and correspond to the same experimental conditions. At t=0 s the surface temperature distribution for all three surfaces is similar, however, the peak in local heat flux for the SH case is 29% lower than for the HPi surface and

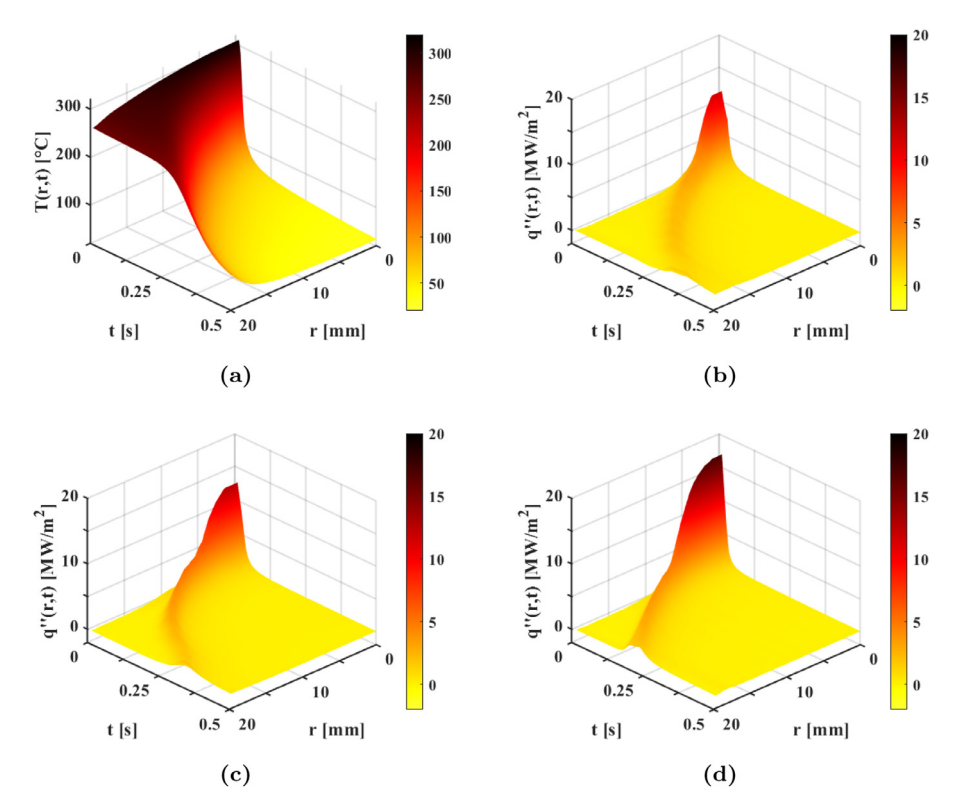


Fig. 8. Surface temperature (T(r,t)) and heat flux (q''(r,t)) data at $T_0 = 320$ °C and $Re_D = 12,000$. (a) Wafer surface temperature as a function of radius and time for the SH surface. (b–d) Heat flux as a function of radius and time for the SH (b), HPo (c), and HPi (d) surfaces.

the jet spreads the slowest across it. There exists a negligible radial temperature gradient near the stagnation region at $t=0\,$ s, although large temporal temperature gradients exist at larger r that differ significantly for the three surfaces.

Fig. 9 b again illustrates that while the thin films on the HPi and HPo surfaces have spread to nearly the same radial location ($r=7-8\,$ mm) by $t=0.05\,$ s, on the SH surface the thin film remains confined to $r\leq 4\,$ mm. Consequently, there is a much smaller area that has been cooled by the jet. By $t=0.15\,$ s (panel c), much of the surface has been cooled to subcritical temperatures, and the peak local heat flux is greatly diminished for all surfaces.

To further connect the heat transfer behavior to the thin film hydrodynamics, the total normalized energy transferred from the wafer $(\hat{E}(t))$ was computed using Eq. (2). Fig. 10a provides data illustrating the differences in $\hat{E}(t)$ between surface types for the two extreme T_0 values considered and at $Re_D=12,000$. Initially, significant thermal energy is transferred to the jet, indicated by the steep slope of the \hat{E} vs. t curve. The curve then begins to level off as much of the surface has cooled and the temperature is no longer changing significantly in time. This is concomitant with a transition from latent to sensible energy transfer as the entire surface cools, boiling ceases, and single-phase convection becomes the dominant mode of heat transfer.

Due to high spatial temperature gradients, $\hat{E}(t)$ can exceed unity at large t. Values of $\hat{E}(t)$ in excess of unity result because of conjugate heat transfer as thermal energy is conducted through the wafer from outside the r_{lim} region. This is especially true for SH and HPo surfaces, where the thin film spreads more slowly (see Fig. 6a). The slope of the $\hat{E}(t)$ curves corresponds to the initial normalized heat transfer rate, which is relatively constant for a significant portion of the total quenching time. Fig. 10a shows that heat transfer is greater at $T_0 = 200$ °C than at $T_0 = 320$ °C for all surface types, indicated by the steeper slopes for corresponding lower-temperature cases, which will be quantified later. Fig. 10b

shows the differences in $\hat{E}(t)$ for the two extreme Re_D cases considered ($T_0 = 280~^{\circ}\text{C}$). Although not shown, the Re_D = 12,000 data is nominally midway between the Re_D = 6000 and 18,000 scenarios. Once again, the normalized energy transfer is initially high (steep gradients). At low Re_D, the $\hat{E}(t)$ curve changes gradually with time. In contrast, at Re_D = 18,000 it changes much more abruptly due to the much faster quenching. As was mentioned previously, at Re_D = 6000 the maximum radius where the thin film breaks up into droplets is smaller than r_{lim} . A result of this is that the initial thermal energy stored in the wafer is not completely removed over the time frame explored. This is demonstrated by the $\hat{E}(t)$ curves not reaching a value of unity in Fig. 10b.

The data of Fig. 10 also shows that surface type impacts heat transfer significantly. At all Re_D and T_0 conditions tested, thermal transport to the jet is slowest for the SH surface and most rapid for HPi surface. At Re_D = 12,000 (Fig. 10a), the HPo data lies nearly halfway between the data for the SH and HPi surfaces. However, at Re_D = 6000 (Fig. 10b), the behavior for the HPo surface is more similar to the SH surface. In contrast, at higher values of Re_D (18,000), the energy transfer rates for the HPo and HPi surfaces are similar.

The temporal derivative of E(t) provides an average rate of the heat transfer throughout time over the area of the viewing window ($0 \le r \le 20$ mm). To quantify the qualitative results shown in Fig. 10, initial rates of heat transfer were determined by evaluating the temporal derivative of the first 0.05 to 0.3 s of E(t) data. The gradient was determined for all cases over the time period where the E(t) vs. t curves were linear. Shown in Fig. 11a is the initial heat rate, \bar{q}_0 , (in units of W) plotted as a function of T_0 (horizontal axis) for all surface types (denoted by marker shape) and at $Re_D = 12,000$. Similarly Fig. 11b provides the heat rate as a function of jet Re_D for all three surface types at $T_0 = 280$ °C. The general behavior is discussed below with regard to T_0 and Re_D and this is followed by an analysis of the influence of the surface type.

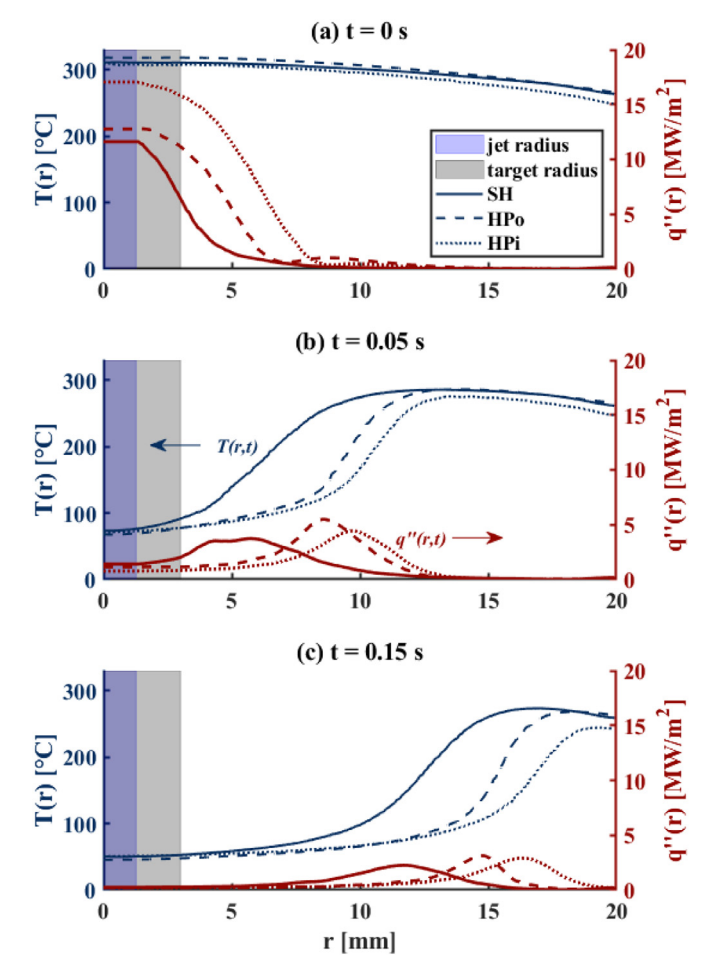


Fig. 9. Temperature (left axis) and local heat flux (right axis) as a function of radius at (a) t=0 s, (b) 0.05 s, and (c) 0.15 s for $T_0=320$ °C and Re_D = 12,000. SH surfaces clearly have the lowest initial heat flux values, and cool the slowest.

The initial heat transfer rate is influenced by competing effects due to varying T_0 , leading to the results shown in Fig. 11a. As T_0 increases, more initial energy is available to be transferred and higher temperature differences between the jet and the wafer exist. However, elevated temperatures also result in slower thin film spreading due to boiling at the edge of the thin film that inhibits spreading. The combination of these two competing effects results in heat transfer rates for the SH and HPo surfaces that vary only modestly with T_0 . However, for the HPi surface, at $T_0 = 200$ °C the heat transfer rate is more than three times higher than for other initial temperatures. This occurs because the Leidenfrost point has not been reached for this surface type and thus the thin film spreads notably faster as the surface does not need to cool as much in order for water to be in good contact over the entire thin film region (see corresponding $\hat{E}(t)$ curve in Fig. 10a).

In contrast to the competing effects of T_0 , increasing the jet Re_D increases the initial heat rate for all cases. This is illustrated in the results of Fig. 11b. Increasing Re_D always yields faster thin film spreading (see Fig. 6b), which directly impacts the rate at which heat is transferred from the surface to the wafer.

The data of Fig. 11a and b also reveals that surface type exercises significant influence on the initial heat transfer rates. In general, the heat transfer rate for the HPi surface is consistently higher than that for the SH surface with corresponding experimental conditions, which correlates to the steeper gradients seen in Fig. 10. As noted above, at $T_0 = 200\,^{\circ}\text{C}$ and $\text{Re}_D = 12,000$, the heat transfer rate for the HPi surface is nominally three times greater than

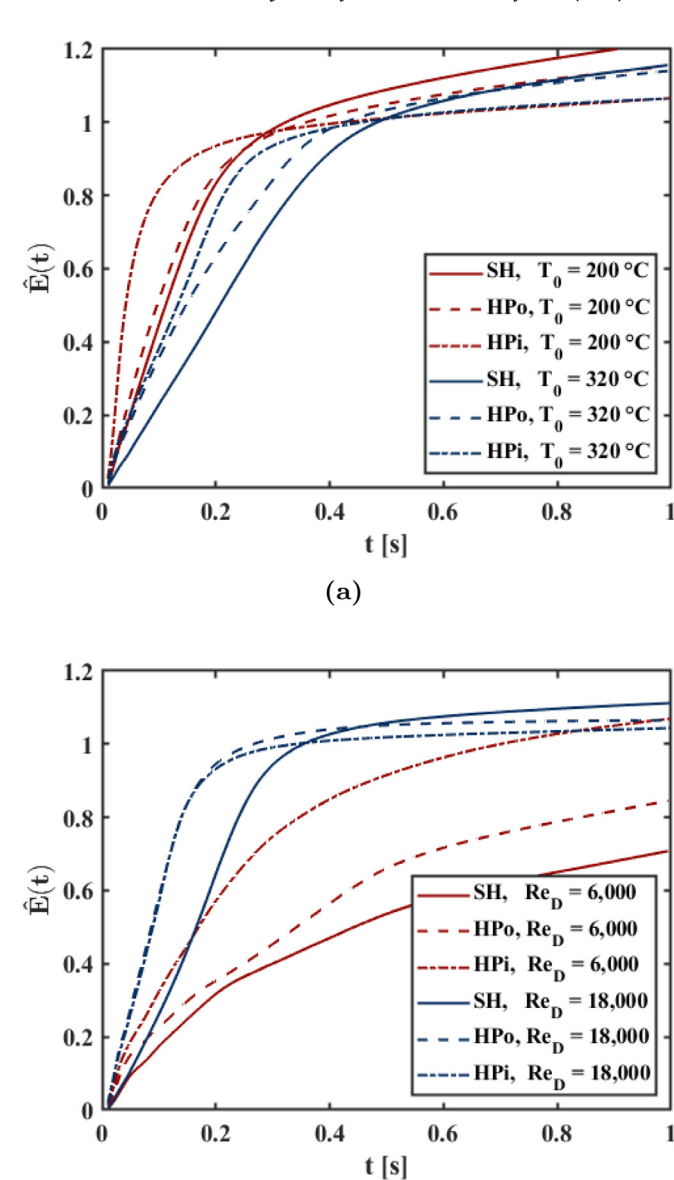


Fig. 10. Normalized thermal energy transferred as a function of time for varying (a) T_0 (Re_D = 12,000) and (b) Re_D (T_0 = 280 °C).

(b)

for the HPo surface and approximately four times greater than for the SH surface. At $T_0 = 280$ and 320 °C the respective heat rates for the HPi surface are approximately 30 and 50% greater than for the SH surface. These results support the idea that increased hydrophobicity preserves or enhances Leidenfrost behavior, even at lower temperatures. The initial heat transfer rates for the HPo surface yield values similar to those of SH surfaces at some conditions, but closer to the HPi surface results for other conditions. At $Re_D = 6000$ and $T_0 = 280$ °C the initial heat rate for the HPo and SH surfaces are nominally the same and are approximately 40% lower than for the HPi case. In contrast, at this same T_0 at Re_D = 18,000, the results for the HPo and HPi surfaces are nearly identical, although the heat rate for the SH surface is approximately 40% lower. This transition in behavior is not entirely understood, but it is likely caused by competing hydrodynamic and thermal effects associated with each of the surface types. The SH and HPo surfaces in general yield hydrodynamic behavior that tends to be more similar than the HPi surface. However, the HPo and HPi surfaces are

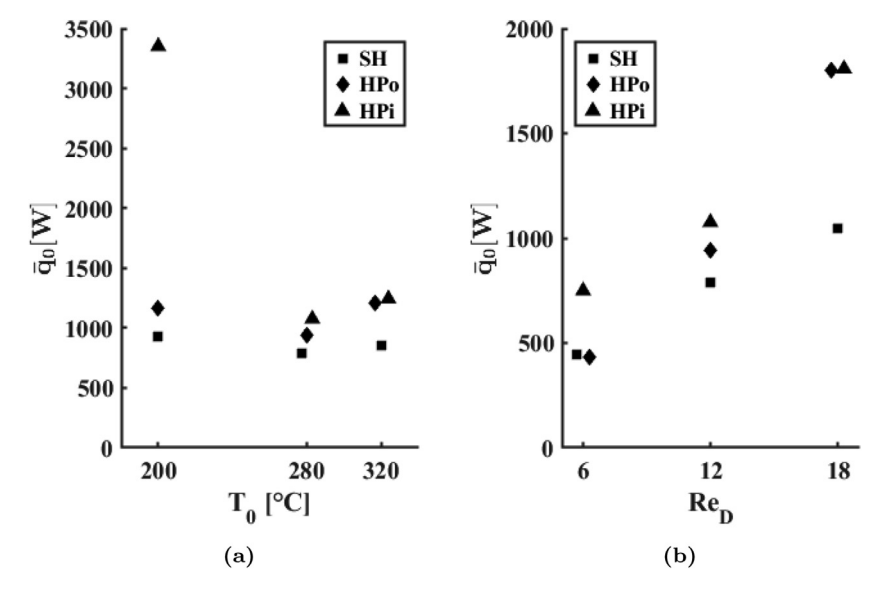


Fig. 11. Initial average heat rates as a function of (a) T_0 (Re_D = 12,000), and (b) jet Re_D (T_0 = 280 °C).

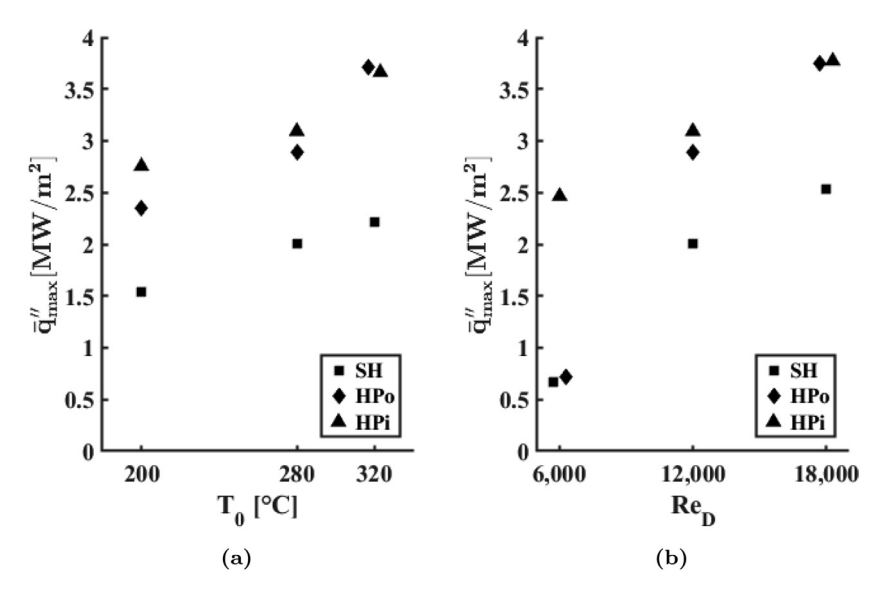


Fig. 12. Values of \bar{q}''_{max} as a function of (a) T_0 (at $Re_D=12,000$) and (b) jet Re_D (at $T_0=280$ °C), for all surface types.

both smooth and do not have underlying cavities that inherently reduce heat transfer and enhance Leidenfrost behavior.

The initial average heat rates discussed above provides insight into differences in heat transfer behavior for the various surface types, T_0 , and Re_D explored. However, local heat flux values also add insight into the thermal transport from the surface to the jet, as was shown in Figs. 8 and 9. At radial locations beyond $r \approx 6$ mm, the instantaneous maximum local heat flux on a surface decreases uniformly as the peak moves outward radially with increasing time. This is shown by the peaks in heat flux in Fig. 8bd. Because this local maximum heat flux varies with time and occurs at different radial locations as the thin film spreads, here we condense the data for simpler comparison and provide another metric of heat transfer comparison between the three surface types. To do this the maximum local heat flux values were averaged over the time period that corresponds to when the peak moved from r = 6 to r = 20 mm. These averaged maximum heat flux values ($\bar{q}''_{\rm max}$) are shown as functions of T_0 in Fig. 12a at Re_D = 12,000, with the three surface types delineated by different markers, similar to Fig. 11a. In contrast to the initial total heat rate

comparison, there is a definitive increase in \bar{q}''_{max} with increasing T_0 , showing strong dependence on the driving temperature difference. Fig. 12b shows \bar{q}''_{max} as a function of Re_D at $T_0 = 280$ °C. A general trend of increasing \bar{q}''_{max} with increasing Re_D is also evident, regardless of surface type, similar to the initial heat rate data

The data displayed in Fig. 12a and b clearly shows that \bar{q}''_{max} for the HPi surface is always significantly higher than for the SH surfaces. The largest difference can be seen at the lowest Re_D, where \bar{q}''_{max} is 263% higher for the HPi surface than for the SH surface. The average difference for the other conditions is nominally 1.2 MW/m², corresponding to values that are 50–80% higher on the HPi surface. In fact, the flow rate for impingement on the SH surface must be nearly triple that of HPi surfaces to reach approximately the same \bar{q}''_{max} value.

The values of $\bar{q}_{\max}^{"'}$ for the HPo surface show similar variability as the initial heat rate values discussed above. At Re_D = 6000, $\bar{q}_{\max}^{"}$ for the HPo and SH surfaces are similar. And, at the maximum Re_D and T_0 values considered, $\bar{q}_{\max}^{"}$ for the HPo and HPi surfaces are nominally the same. As noted above, this changing dynamic is

likely due to competing hydrodynamic and thermal characteristics of the surfaces.

4. Conclusions

Jet impingement quenching of superheated smooth HPi ($\theta=55^\circ$), smooth HPo ($\theta=123^\circ$) and micropost-patterned SH ($\theta=155^\circ$) surfaces was investigated. Initial surface temperature was varied from $T_0=200$ to 320 °C and jet Reynolds numbers of ReD = 6000, 12,000, and 18,000 were explored. Typical jet quenching behavior was observed for all cases, including the rapid formation of a convective liquid thin film bounded by a region of vigorous boiling and localized high heat flux. Conclusions about heat transfer can be drawn based on the three parameters varied: T_0 , jet ReD, and surface type.

Results from this study show that for increasing T_0 the spreading of the jet thin film is impeded on all surface types. This is due to rapid vaporization creating a barrier to liquid-surface contact and yielding high localized heat transfer. However, the increased temperature also increases the driving potential for heat transfer, resulting in higher local heat fluxes. Increased driving temperature difference and impeded thin film spreading result in competing influences on average heat transfer rate over the surface.

Increasing jet Re_D adds fluid momentum that can overcome the effects that impede thermal transport, leading to faster and farther thin film spreading. This was reflected in the numerical heat transfer comparisons of heat flux and heat rate, which both increased an average of 200% for all surface types when jet Re_D was increased from 6000 to 18,000.

Finally, surface type was shown to have a large impact on jet impingement heat transfer. The thin film spread more slowly on the SH surfaces compared to HPi and HPo cases due to an enhanced Leidenfrost effect, which also lowered the heat transfer rate. Quantitative comparisons between the SH and HPi surfaces showed the former had up to 70% lower values of both averaged maximum heat flux and initial total heat rate.

Declaration of Competing Interest

The authors declare that they have no known competing financial interests or personal relationships that could have appeared to influence the work reported in this paper.

CRediT authorship contribution statement

D. Jacob Butterfield: Conceptualization, Formal analysis, Funding acquisition, Data curation, Writing - original draft, Validation. **Brian D. Iverson:** Conceptualization, Data curation, Formal analysis, Writing - review & editing, Validation, Funding acquisition. **Daniel Maynes:** Conceptualization, Data curation, Formal analysis, Writing - review & editing, Validation, Funding acquisition. **Julie Crockett:** Conceptualization, Data curation, Formal analysis, Writing - review & editing, Validation, Funding acquisition.

Acknowledgments

The authors recognize the assistance provided by Benjamin Johnson in fabricating many of the surfaces used in this work, and Cole Thatcher, who performed many of the experiments. Funding for this research has been supported by the National Science Foundation [grant number: CBET-1707123] and by the Utah NASA Space Grant Consortium.

References

[1] J.H. Lienhard, Liquid jet impingement, Annu. Rev. Heat Transf. 6 (6) (1995) 199–270, doi:10.1615/AnnualRevHeatTransfer.v6.60.

- [2] J. Filipovic, F.P. Incropera, R. Viskanta, Quenching phenomena associated with a water wall jet: II. Comparison of experimental and theoretical results for the film boiling region, Exp. Heat Transf. 8 (2) (1995) 119–130.
- [3] G. Nasif, R. Barron, R. Balachandar, The application of jet impingement for piston cooling, in: 11th International Conference on Heat Transfer, Fluid Mechanics and Thermodynamics, 2015, pp. 481–486.
- [4] B. Han, R.J. Goldstein, Jet-impingement heat transfer in gas turbine systems, Ann. The New York Acad. Sci. 934 (2001) 147–161, doi:10.1111/j.1749-6632. 2001.tb05849.x. https://nyaspubs.onlinelibrary.wiley.com/.
- [5] N. Karwa, P. Stephan, Experimental investigation of free-surface jet impingement quenching process, Int. J. Heat Mass Transf. 64 (2013) 1118–1126, doi:10. 1016/i.jiheatmasstransfer.2013.05.014.
- [6] M.M. Awad, Fouling of heat transfer surfaces, in: A. Belmiloudi (Ed.), Heat Transfer - Theoretical Analysis, Experimental Investigations and Industrial Systems, InTech, 2011, pp. 505–542.
- [7] P. Zhang, F.Y. Lv, A review of the recent advances in superhydrophobic surfaces and the emerging energy-related applications, Energy 82 (2015) 1068–1087, doi:10.1016/j.energy.2015.01.061. http://www.sciencedirect.com/science/article/ pii/S0360544215000857.
- [8] J.F. Prince, D. Maynes, J. Crockett, On jet impingement and thin film breakup on a horizontal superhydrophobic surface, Phys. Fluids 27 (11) (2015), doi:10. 1063/1.4935498. http://aip.scitation.org/toc/phf/27/11.
- [9] M. Searle, D. Maynes, J. Crockett, Thermal transport due to liquid jet impingement on superhydrophobic surfaces with isotropic slip, Int. J. Heat Mass Transf. (2017) 680–691, doi:10.1016/j.ijheatmasstransfer.2017.03.044.
- [10] B.W. Webb, C.F. Ma, Single-phase liquid jet impingement heat transfer, Adv. Heat Transf. 26 (1995) 105–217.
- [11] X. Liu, J.H. Lienhard, Liquid jet impingement heat transfer on a uniform flux surface, HTD 106 (1989) 523-529. http://web.mit.edu/lienhard/www/papers/ conf/LIU-Liquid-jet-impingement-heat-transfer-on-a-uniform-flux-surface-AS ME-1989.pdf.
- [12] X. Liu, J.H. Lienhard, J.S. Lombara, Convective heat transfer by impingement of circular liquid jets, J. Heat Transf. 113 (3) (1991) 571, doi:10. 1115/1.2910604. http://heattransfer.asmedigitalcollection.asme.org/article.aspx? articleid=1440779.
- [13] K. Jambunathan, E. Lai, M.A. Moss, B.L. Button, A review of heat transfer data for single circular jet impingement, Int. J. Heat Fluid Flow 13 (2) (1992) 106– 115, doi:10.1016/0142-727X(92)90017-4.
- [14] B. Elison, B.W. Webb, Local heat transfer to impinging liquid jets in the initially laminar, transitional, and turbulent regimes, Int. J. Heat Mass Transf. 37 (8) (1994) 1207–1216, doi:10.1207/s15327752jpa8502.
- [15] H. Robidou, H. Auracher, P. Gardin, M. Lebouché, et al., Controlled cooling of a hot plate with a water jet, Exp. Therm. Fluid Sci. 26 (2-4) (2002) 123–129, doi:10.1016/S0894-1777(02)00118-8.
- [16] M. Monde, Y. Katto, Burnout in a high heat-flux boiling system with an impinging jet, Int. J. Heat Mass Transf. 21 (3) (1978) 295–305, doi:10.1016/0017-9310(78)90122-9.
- [17] J. Kokado, N. Hatta, H. Takuda, J. Harada, N. Yasuhira, et al., An analysis of film boiling phenomena of subcooled water spreading radially on a hot steel plate, Arch. Eisenhüttenwesen 55 (3) (1984) 113–118, doi:10.1002/srin. 108405320
- [18] M. Monde, Critical heat flux in saturated forced convection boiling on a heated disk with an impinging jet, J. Heat Transf. 109 (1987) 991– 996
- [19] Z. Liu, J. Wang, Study on film boiling heat transfer for water jet impinging on high temperature flat plate, Int. J. Heat Mass Transf. 44 (13) (2001) 2475–2481, doi:10.1016/S0017-9310(00)00281-7.
- [20] C. Kamata, Experimental study on boiling heat transfer with an impinging jet on a hot block, Heat Transf. Asian Res. 28 (5) (1999) 418–427, doi:10.1252/ kakoronbunshu.23.526.
- [21] W. Timm, K. Weinzierl, A. Leipertz, Heat transfer in subcooled jet impingement boiling at high wall temperatures, Int. J. Heat Mass Transf. 46 (8) (2003) 1385– 1393, doi:10.1016/S0017-9310(02)00416-7.
- [22] N. Seiler-Marie, J.M. Seiler, O. Simonin, Transition boiling at jet impingement, Int. J. Heat Mass Transf. 47 (23) (2004) 5059–5070, doi:10.1016/j.ijheatmasstransfer.2004.06.009.
- [23] A.H. Nobari, V. Prodanovic, M. Militzer, Heat transfer of a stationary steel plate during water jet impingement cooling, Int. J. Heat Mass Transf. 101 (2016) 1138–1150, doi:10.1016/j.ijheatmasstransfer.2016.05.108.
- [24] L. Qiu, S. Dubey, F.H. Choo, F. Duan, Recent developments of jet impingement nucleate boiling, 2015. doi:10.1016/j.ijheatmasstransfer.2015.05.025.
- [25] Y. Mitsutake, M. Monde, Heat transfer during transient cooling of high temperature surface with an impinging jet, Heat Mass Transf. 37 (4-5) (2001) 321– 328, doi:10.1007/s002310000141.
- [26] M.A. Islam, M. Monde, P.L. Woodfield, Y. Mitsutake, et al., Jet impingement quenching phenomena for hot surfaces well above the limiting temperature for solid-liquid contact, Int. J. Heat Mass Transf. 51 (5-6) (2008) 1226–1237, doi:10.1016/j.ijheatmasstransfer.2007.01.059.
- [27] H. Leocadio, C.W.M. Van Der Geld, J.C. Passos, Rewetting and boiling in jet impingement on high temperature steel surface, Phys. Fluids 30 (12) (2018) 122102, doi:10.1063/1.5054870.
- [28] A.K. Sharma, M. Modak, S.K. Sahu, The heat transfer characteristics and rewetting behavior of hot horizontal downward facing surface by round water jet impingement, Appl. Therm. Eng. 138 (2018) 603–617, doi:10.1016/j.applthermaleng.2018.04.050. https://linkinghub.elsevier.com/ retrieve/pii/S1359431117349256.

- [29] T. Ochi, S. Nakanishi, M. Kaji, S. Ishigai, et al., Multi-Phase Flow and Heat Transfer III. Part A: Fundamentals "Cooling of a Hot Plate with an Impinging Circular Water Jet", Elsevier Science Publishers B.V., Amsterdam, 1984.
- [30] D.E. Hall, F.P. Incropera, R. Viskanta, et al., Jet impingement boiling from a circular free-surface jet during quenching: part 1 - single-phase jet, J. Heat Transf. 123 (5) (2001) 911, doi:10.1115/1.1389062. http://heattransfer. asmedigitalcollection.asme.org/article.aspx?articleid=1445200.
- [31] S. Kumagai, S. Suzuki, Y. Sano, M. Kawazoe, et al., Transient cooling of a hot metal plate with an impinging water jet, in: ASME/JSME Thermal Engineering Conference, volume 2, 1995, pp. 347–352.
- [32] S. Ishigai, S. Nakanishi, T. Ochi, Boiling heat transfer for a plane water jet impinging on a hot surface, in: 6th International Heat Transfer Conference, Toronto, 1978, pp. 445–450.
- [33] S. Waldeck, U. Fritsching, Heat transfer in the boiling regime of impinging liquid jets, 2nd World Congress on Momentum, Heat and Mass Transfer, Barcelona, Spain, 2017, doi:10.11159/icmfht17.128.
- [34] C.E. Clavijo, J. Crockett, D. Maynes, Hydrodynamics of droplet impingement on hot surfaces of varying wettability, Int. J. Heat Mass Transf. 108 (2017) 1714– 1726, doi:10.1016/j.ijheatmasstransfer.2016.12.076.
- [35] I.U. Vakarelski, N.A. Patankar, J.O. Marston, D.Y.C. Chan, S.T. Thoroddsen, et al., Stabilization of Leidenfrost vapour layer by textured superhydrophobic surfaces, Nature 489 (7415) (2012) 274–277, doi:10.1038/nature11418. https://www.nature.com/articles/nature11418.pdf. NIHMS150003.
- [36] M. Searle, P. Emerson, J. Crockett, D. Maynes, Influence of microstructure geometry on pool boiling at superhydrophobic surfaces, Int. J. Heat Mass Transf. 127 (2018) 772–783, doi:10.1016/j.ijheatmasstransfer.2018.07.044.

- [37] A. Cowley, D. Maynes, J. Crockett, B.D. Iverson, Bubble nucleation in superhydrophobic microchannels due to subcritical heating, Int. J. Heat Mass Transf. 121 (2018) 196–206, doi:10.1016/j.ijheatmasstransfer.2017.03.055.
- [38] Y. Qiu, Z. Liu, Nucleate boiling on the superhydrophilic surface with a small water impingement jet, Int. J. Heat Mass Transf. 51 (7-8) (2008) 1683–1690, doi:10.1016/j.ijheatmasstransfer.2007.07.049. http://www.elsevier. com/locate/lihmt.
- [39] M.C. Searle, Thermal Transport at Superhydrophobic Surfaces in Impinging Liquid Jets, Natural Convection, and Pool Boiling, Brigham Young University, 2018 Ph.D. thesis.
- [40] S.G. Lee, M. Kaviany, C.J. Kim, J. Lee, Quasi-steady front in quench subcooled-jet impingement boiling: experiment and analysis, Int. J. Heat Mass Transf. 113 (2017) 622–634, doi:10.1016/j.ijheatmasstransfer.2017.05.081.
- [41] A.K. Mozumder, M. Monde, P.L. Woodfield, M.A. Islam, et al., Maximum heat flux in relation to quenching of a high temperature surface with liquid jet impingement, Int. J. Heat Mass Transf. 49 (17-18) (2006) 2877–2888, doi:10.1016/j.ijheatmasstransfer.2006.01.048. http://www.elsevier.com/locate/ijhmt.
- [42] J. Hammad, Y. Mitsutake, M. Monde, Movement of maximum heat flux and wetting front during quenching of hot cylindrical block, Int. J. Therm. Sci. 43 (8 SPEC. ISS.) (2004) 743–752, doi:10.1016/j.ijthermalsci.2004.02.014. http://www. elsevier.com/locate/ijts.